Optics Communications 586 (2025) 131871

Contents lists available at ScienceDirect

Optics Communications

journal homepage: www.elsevier.com/locate/optcom

Temperature-insensitive parallel dual FPI strain sensor based on the vernier effect

Wei Li [a], Jingwei Lv [a,*], Xili Lu [b], Chao Liu [a], Renfeng Li [a], Liangliang Li [a], Weijie Kong [a], Qiang Liu [a], Jianing Shi [a], Wei Liu [a], Pan Meng [a], Xinrui Guo [a], Paul K. Chu [c]

[a] School of Physics and Electronic Engineering, Northeast Petroleum University, Daqing, 163318, PR China
[b] School of Materials Science and Chemical Engineering, Harbin Engineering University, Harbin, 150001, PR China
[c] Department of Physics, Department of Materials Science and Engineering, and Department of Biomedical Engineering, City University of Hong Kong, Tat Chee Avenue, Kowloon, Hong Kong, China

ARTICLE INFO

Keywords:
Fabry-pérot interferometer
Vernier effect
Optical fiber sensor
Strain sensitivity
Temperature cross-sensitivity

ABSTRACT

A temperature-insensitive Fabry-Pérot interferometer (FPI) based on the Vernier effect is proposed for strain measurement. Two structurally similar FPIs are prepared with a fusion splicer, and the air cavity in the middle forms the Fabry-Pérot cavity. The one FPI with a thinner wall serves as the sensing cavity, and the other is the reference cavity. The strain sensitivity of the optical fiber sensor for 0–600 με is 131.7 pm/με, which is 9 times higher than that of the single structure FPI. It has a temperature sensitivity of 2.7 pm/°C and a temperature cross-sensitivity of 0.021 με/°C in the temperature range between 25 and 200 °C. The sensor has excellent repeatability and stability in strain measurements. The results show that the strain sensor is simple, cost-effective, and easy to fabricate. In conjunction with its high sensitivity, it has great commercial potential in strain measurements, especially in complex temperature environments.

1. Introduction

Precise strain measurements are important to the maintenance and repair of bridges, aircraft wings, and pipelines [1–4], and optical fiber-based devices are attractive due to their flexibility, geometrical versatility, and electromagnetic immunity [5,6]. There are several types of strain sensors such as Fabry-Pérot interferometers (FPI) [7,8], fiber Bragg gratings (FBG) [9,10], Mach-Zender interferometers (MZI) [11–13], and others. Among them, FPI has a simple structure and is less susceptible to temperature variations. Hence, it is easier to miniaturize than other types of sensors for strain measurements [14]. Tian et al. have embedded a microsphere inside a tapered hollow core fiber (HCF) by the fiber tip capture method and changed the cavity length of the FPI by controlling the diameter of the tapered HCF and the size of the embedded microsphere to increase the extinction ratio of the reflectance spectra and to improve the sensitivity of the sensor [15]. Su et al. have fabricated a hybrid fiber FPI based on HCF-FMF-SMF, in which a few-mode fiber (FMF) bias splices the single-mode fiber (SMF) to excite higher-order modes in the core [16]. However, the preparation of these sensors tends to be expensive and complex, and the sensitivity of only 16.2 pm/με is not satisfactory.

The Vernier effect can be adopted by optical fiber interferometers to improve the sensitivity and resolution of sensors [17]. This effect relies on the overlap between the signals of two interferometers with slightly detuned interference frequencies, namely the reference interferometer (RI) and sensing interferometer (SI). Vernier effect-based spectra generation by Vernier envelope modulation exhibits an amplified spectral drift compared to single-structure interferometers, leading to a new generation of highly sensitive fiber optic sensors [18]. Optical fiber sensors based on the Vernier effect offer have been used to monitor strain, gas pressure, and refractive indexes [19–21].

Herein, a temperature-insensitive optical fiber strain sensor is prepared with air-bubble-based FPI based on the optical Vernier effect. The microbubbles inside the single-mode fiber form the RI and SI with different cavity lengths using an economical and simple fiber fusion splicing technique. They are connected in parallel to form the sensor. The experimental results demonstrate that the sensor has a strain sensitivity of 131.7 pm/με in the range of 0–600 με, which is enhanced by a factor of 9 compared to the single-structure FPI. The temperature sensitivity and temperature cross-sensitivity are 2.7 pm/°C and 0.021

* Corresponding author.
E-mail address: lvjingwei2009123@126.com (J. Lv).

https://doi.org/10.1016/j.optcom.2025.131871
Received 16 December 2024; Received in revised form 4 April 2025; Accepted 12 April 2025
Available online 16 April 2025

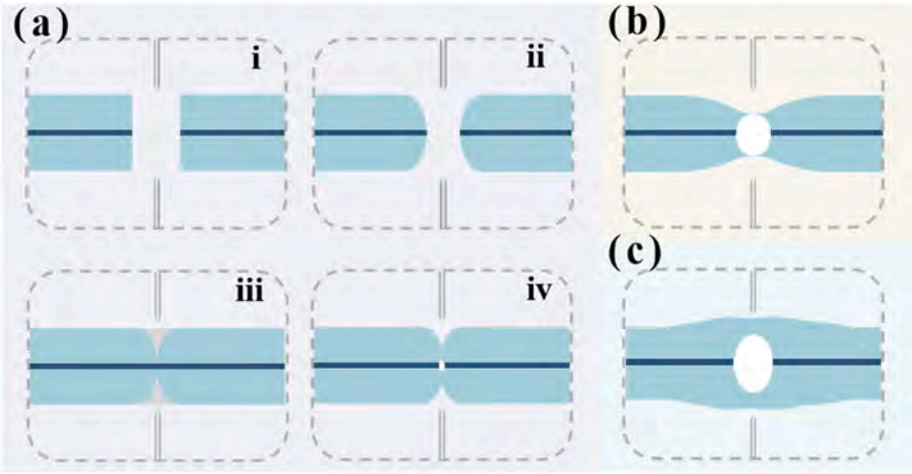

Fig. 1. Schematic diagram of the fabrication process: (a) Pre-processing, (b) SI, and (b) RI.

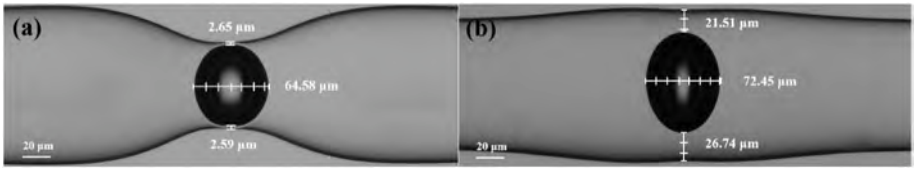

Fig. 2. Optical images of (a) SI and (b) RI.

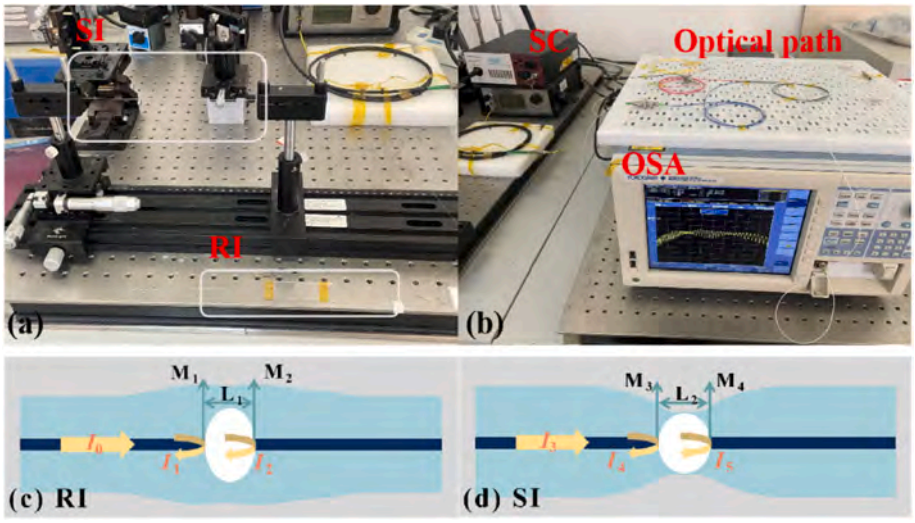

Fig. 3. (a) RI, SI, and 3D moving platform, (b) SC light source, OSA, and optical path with 3 dB coupler, (c) RI sensing principle, and (d) SI sensing principle.

με/°C in the temperature range of 25–200 °C, respectively. In addition, the sensor has small temperature crosstalk as well as excellent repeatability and stability boding well for micro-strain detection.

2. Sensor fabrication and principle

The free spectral range equation of the FPI is adopted to design the FSR and cavity length of the FPI. The fabrication process of the sensor is shown in Fig. 1. In brief, one end of the two SMF segments is cut flat and placed in a commercial fusion splicer (Fujikura 80s). The fiber end is reshaped into a rounded curved surface by arc discharge to increase the surface area. One fiber is removed and dipped into a small amount of matching fluid to promote microbubble formation. Finally, the stepper motors are moved to squeeze the optical fibers slightly, and the microbubble is produced by an arc discharge.

The fabrication process of SI is shown in Fig. 1(b). The sensing FPI with a thinner wall is obtained by increasing the discharge power and time of the fusion splicer and shaping the stress on the basis of the small air bubble. The optical micrograph and parameters of the high-sensitivity FPI are shown in Fig. 2(a). The thickness of the narrowest part of the bubble wall is 2.59 μm, and the axial air bubble length is 64.58 μm. The thinner bubble thickness can make the strain effect more concentrated and get higher strain sensitivity. The fabrication process of the RI is shown in Fig. 1(c). The axial tension described in Fig. 1(iv) yields a larger bubble, which is made gradually smaller by squeezing for a short period of time until it matches SI. The optical micrograph and parameters of the low-sensitivity FPI for the Vernier effect are presented in Fig. 2(a). The average wall thickness of the bubble is 21.51 μm, and

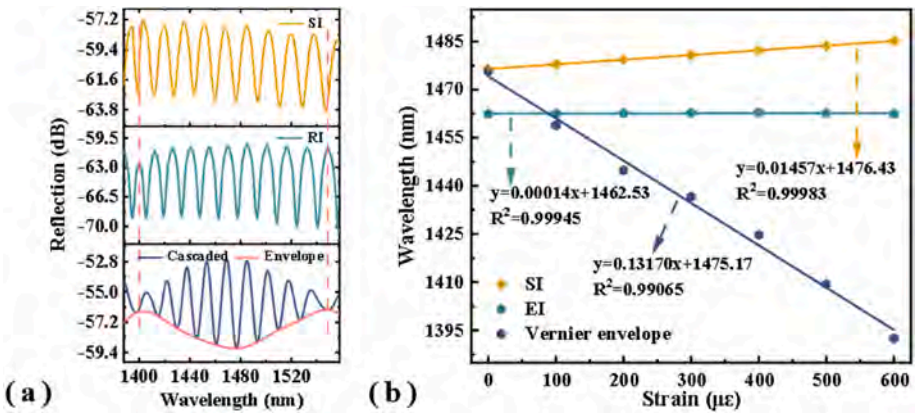

Fig. 4. (a) Output spectra and (b) Linear fitting of SI, RI, and cascade spectra.

the axial length is 72.45 μm. The method of fabricating the sensor using a fusion splicer is simple, cost-effective, and flexible and reproducible (see S1 in the Supplementary file for the exact validation of production reproducibility, and see S2 for the effect of these sizes variations on the strain sensitivity and temperature of the sensors).

The schematic diagram of the experimental setup of the axial strain sensor consisting of a sensing arm and a reference arm is depicted in Fig. 3(a) and (b). The output from a continuous light source (SC, 450–2500 nm) is introduced into the two parallel FPIs through a 3 dB coupler, and the reflected beam is received by an optical spectrum analyzer (OSA) with a resolution of 0.02 nm to record the spectrum. The RI is fixed on a slide to ensure that it will not be disturbed by the external environment. The SI is straightened and fixed on the two 3D moving platforms with a distance of 20 cm so that the axial strain applied to the sensor is 100 με at a time. As the axial strain increases, the bubble inside the SI undergoes micro-deformation, which changes the reflection spectrum collected by the OSA in real time. The SI has a small wall thickness so that the strain can act more effectively on the air bubble. In this case, M_1 and M_2 are the two reflective surfaces of the RI with reflection intensities I_1 and I_2, and L_1 is the cavity length of the reference cavity. Similarly, M_3 and M_4 are the two reflective surfaces of SI with reflective intensities I_4 and I_5, and L_2 is the cavity length of the sensing cavity. Unlike the SI, the thickness of the bubble wall is artificially increased during the fabrication of the RI to minimize the possibility of strain interferences.

For illustration, the sensing principle is described for RI. The intensity of the light emitted from the SC arrives at the reflective surface M_1 is I_0, and the intensity of the first reflection is I_1. A part of the light passes through M_1 to reach the reflective surface M_2 for the second reflection, and the intensity of the reflection is I_2. The two reflected light beams are coupled in the fiber core to generate interference. The intensity of the reflected light can be expressed as follows:

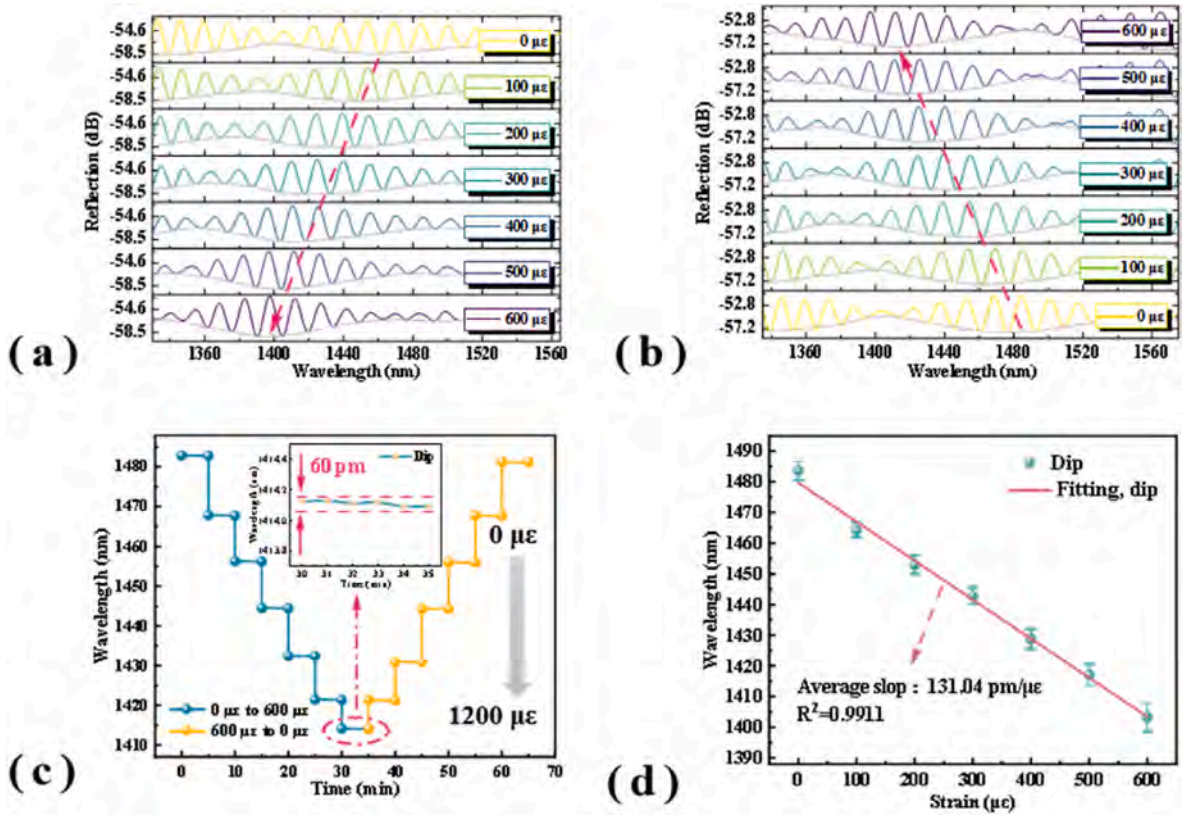

Fig. 5. Vernier envelope results: (a) Forward strain, (b) Reverse strain, (c) Forward and reverse stability, and (d) Forward repeatability.

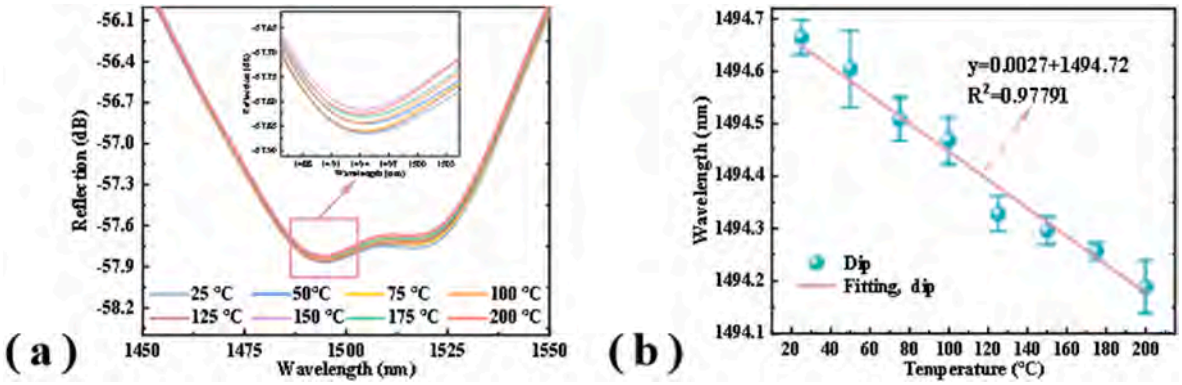

Fig. 6. Temperature response: (a) Reflection spectra of the sensor at different temperatures and (b) Relationship between the dip wavelength shift and temperature.

$$I_0 = I_1 + I_2 + 2\sqrt{I_1 I_2}COS(\theta), \tag{1}$$

where θ is the phase difference caused by light transmitted in the cavity. In the case of two-beam interference, the reflection spectrum exhibits cosine characteristics. The distance between two neighboring resonance dips in the interference spectrum is called the free spectral range (FSR), which can be obtained by calculating the wavelengths of the two neighboring resonance dips. FSR_R and FSR_S of the reflection spectra are expressed by Eqs. (2) and (3):

$$FSR_R = \lambda_{dip1}(m+1) - \lambda_{dip1}(m) = \frac{\lambda_{dip1}(m+1)\lambda_{dip1}(m)}{2n_{air}L_1} \tag{2}$$

$$FSR_S = \lambda_{dip2}(m+1) - \lambda_{dip2}(m) = \frac{\lambda_{dip2}(m+1)\lambda_{dip2}(m)}{2n_{air}L_2}, \tag{3}$$

where m ($m = 1, 2, 3 \ldots$) denotes the interference order and wavelength at the mth interference dip, and n_{air} is the refractive index of the air in the bubble of the FPI.

When RI and SI have a similar FSR, the interference spectra of two sensors connected in parallel are superimposed to form a large spectral envelope, and the FSR of the envelope is given as:

$$FSR_{envelope} = \frac{FSR_S FSR_R}{|FSR_S - FSR_R|}. \tag{4}$$

The dip wavelength shift of the FSR_S results in a large shift in the dip wavelength of the spectral envelope of the parallel structure when the axial strain changes. The amplification factor M of the wavelength shift is expressed as:

$$M = \frac{FSR_{envelope}}{FSR_S} = \frac{FSR_R}{|FSR_S - FSR_R|}. \tag{5}$$

3. Results and discussion

Fig. 4(a) shows the raw spectra of SI, RI and the complete spectra after cascading in the wavelength range of 1388–1558 nm. The raw spectra of SI and RI basically correspond to a series of clear cosine fringes with comparable interference contrast. The wavelengths corresponding to the dip of SI near 1550 nm are $\lambda_m = 1528.6$ nm and $\lambda_{m+1} = 1547$ nm, respectively, yielding an FSR_S of 18.4 nm. The wavelengths corresponding to RI are $\lambda_m = 1540.6$ nm and $\lambda_{m+1} = 1557.2$ nm, respectively, giving an FSR_R of 16.6 nm. The bubble lengths derived by Eqs. (2) and (3) are $L_1 = 64.26$ nm and $L_2 = 72.26$ nm, respectively, which in general match the bubble lengths determined from the microscopic images in Fig. 2. In the spectra of SI and RI, the phase-opposed distance is $FSR_{envelope} = 166.8$ nm (theoretically $FSR_{envelope} = 169.69$ nm according to Eq. (4)).

Fig. 4(b) shows the strain sensitivity obtained by linear fitting with 0–600 με applied to the sensor in 100 με steps. The wavelengths selected are those corresponding to the dip at different strain levels near 1550 nm, and the strain sensitivities are obtained by linear fitting. The strain sensitivities of the RI and Vernier envelope are 14.57 pm/με and 131.7 pm/με, respectively, and the Vernier structure sensitivity is amplified by 9 times in comparison with the single-structure FPI, which is in good match with the amplification factor obtained by Eq. (5). However, complex environments on experimental platforms such as 3D moving platform or starter for light source inevitably produce slight vibrations that can bias the data, resulting in small changes in the amplification factor of the sensor, as does the post-processing of the experimental data.

The stability and repeatability are evaluated at room temperature, as shown in Fig. 5. Fig. 5(a) and (b) depict the interference spectra of the sensor with axial strain applied in the forward direction from 0 to 600 με, and the reduced strain in the reverse direction. In this experiment, the noise is effectively managed through the use of a high-precision light source and OSA, mechanical isolation, and signal processing. These measures collectively enhance the sensor's measurement accuracy and stability, particularly under rapid strain change conditions. 100 με is added axially to the fiber every 5 min, and the resulting interference spectral changes are recorded until reaching the spectral detection range when the strain gradually decreases to 0 με after 600 με. The dip of the Vernier envelope near 1550 nm for 65 min is recorded, as shown in Fig. 5(c). The maximum fluctuation amounts to merely 60 pm, suggesting that the sensor can maintain stable performance under cyclic loading and is appropriate for long-term monitoring applications. However, during long-term strain measurements, structural relaxation of the air bubble inside the sensor may occur, resulting in a hysteresis between the sensor output and the actual strain. Therefore, the sensor's response time, potential hysteresis effects, and long-term stability under cyclic loading is critical for practical applications where strain changes rapidly.To verify the repeatability, 0–600 με is applied to the sensor under the same conditions five times. The average strain sensitivity of 131.04 pm/με, which is 0.5% different from the actual parameter, confirms the superior repeatability.

The strain sensor is affected by the environment temperature in strain measurements, and it is important to perform precise temperature-insensitive strain sensing. In order to prevent the strain sensor from moving during the experiment, one end of the SI is fixed to a solid iron block using polyimide tape. The SI is then put into a constant temperature dry box, and the RI is kept at room temperature as a reference unit. As shown in Fig. 6(a), the temperature is increased gradually from 25 °C to 200 °C, while the interferometric spectra are acquired at an interval of 25 °C and the dip of the envelope is recorded at the same time. Since the fiber material of the sensor is mainly SiO_2, and SI as well as RI contain only one bubble each, thus the sensor has a low coefficient of thermal expansion and is not affected by the thermal-optical coefficient. As shown in Fig. 6(a), the reflectance spectra remain stable with increasing temperature. The temperature sensitivity of the Vernier envelope is 2.7 pm/°C, while the temperature cross-

Table 1
Comparison between our sensor with previously reported strain sensors.

Types	Temperature cross-sensitivity	Temperature sensitivity	Strain sensitivity	Strain range	References
MZI-FPI by fusion splicer	14.606 με/°C	279.99 pm/°C	19.17 pm/με	0-1350 με	[22] 2023
FPIs by fs laser	9.907 με/°C	278.48 pm/°C	28.11 pm/με	0-1400 με	[23] 2020
FLF-FSI by fusion splicer	1.049 με/°C	61.52 nm/°C	58.63 pm/με	0-4000 με	[24] 2023
FPIs by fusion splicer	0.148 με/°C	6.4 pm/°C	43.2 pm/με	0-1750 με	[25] 2019
CFBG-FPI by fs laser	0.140 με/°C	17.33 pm/°C	123.8 pm/με	0-791με	[26] 2023
FPIs by fusion splicer	0.021 με/°C	2.7 pm/°C	131.7 pm/με	0-600 με	**This work**

sensitivity is 0.021 με/°C after five repetitions of experimental measurements, as shown in Fig. 6(b). The sensor shows a small temperature crosstalk and is almost not affected by the ambient temperature.

To demonstrate the merit and commercial applicability, the characteristics of our sensor are compared with those of similar strain sensors using the Vernier effect in the literature. Since our strain sensor has a double-parallel FPI structure made of SiO_2 and an F–P cavity of air bubbles, the sensor is nearly unaffected by temperature. Meanwhile, the transverse length of the air bubble changes with strain, and the strain sensitivity of a single FPI is amplified by the optical Vernier effect. Consequently, our sensor is more sensitive than strain sensors with the general structure, as shown in Table 1. More importantly, the sensor can be easily fabricated without the need for expensive equipment or hazardous chemicals, thus improving safety and cost-effectiveness.

4. Conclusion

An optical fiber sensing is designed using the Vernier effect for precise and temperature-insensitive strain measurements. The FPI prepared by the fusion splicing method has an adjustable microcavity length, thus reducing the difficulty of matching FSR_S and FSR_R. The experimental results reveal that the sensor has a high strain sensitivity of 131.7 pm/με in the range of 0–600 με, which is 9 times greater than that of the single-structured FPI. The temperature sensitivity and temperature cross-sensitivity of the sensor are 2.7 pm/°C and 0.021 με/°C, respectively, in the temperature range between 25 °C and 200 °C. Moreover, the sensor shows excellent repeatability and stability. Owing to advantages such as small size, low cost, and simple preparation process, the sensor has large commercial potential in micro-strain monitoring.

CRediT authorship contribution statement

Wei Li: Writing – review & editing, Writing – original draft, Software, Methodology. **Jingwei Lv:** Writing – review & editing, Conceptualization. **Xili Lu:** Supervision, Methodology. **Chao Liu:** Validation. **Renfeng Li:** Investigation. **Liangliang Li:** Formal analysis. **Weijie Kong:** Validation, Investigation. **Qiang Liu:** Supervision, Formal analysis. **Jianing Shi:** Data curation. **Wei Liu:** Validation, Supervision. **Pan Meng:** Validation, Software. **Xinrui Guo:** Visualization. **Paul K. Chu:** Project administration.

Declaration of competing interest

The authors declare that they have no known competing financial interests or personal relationships that could have appeared to influence the work reported in this paper.

Acknowledgments

This work was jointly supported by the National Natural Science Foundation of China [12304480], Heilongjiang Provincial Natural Science Foundation of China [JQ2023F001], Local Universities Reformation and Development Personnel Training Supporting Project from Central Authorities, the Basic Research Support Project for the Excellent Youth Scholars of Heilongjiang Province[YQJH2023077], Study Abroad returnees merit-based Aid Foundation in Heilongjiang Province [070-719900103], as well as City University of Hong Kong Donation Research Grants [DON-RMG 9229021 and 9220061].

Appendix A. Supplementary data

Supplementary data to this article can be found online at https://doi.org/10.1016/j.optcom.2025.131871.

Data availability

Data will be made available on request.

References

[1] D. Wang, M. Dong, L. Zhu, X. Lou, M. Yu, Y. Zhang, C. Deng, J. Xin, Y. Zhu, K. Feng, Application of fiber-optic strain sensing technology in high-precision load prediction of aircraft landing gear, Opt Laser. Technol. 182 (2025) 112183.
[2] B. Chen, J. Yang, A. Li, M. Zhang, J. Li, Z. Wang, Strain measurement technology and precision calibration experiment based on flexible sensing fiber, Sensors 24 (12) (2024) 3811.
[3] W. Meng, S.M. Bachilo, R.B. Weisman, S. Nagarajaiah, A review: non-contact and full-field strain mapping methods for experimental mechanics and structural health monitoring, Sensors 24 (20) (2024) 6573.
[4] Z. Guo, J. Xu, Y. Chen, Z. Guo, P. Yu, Y. Liu, J. Zhao, High-sensitive and stretchable resistive strain gauges: parametric design and DIW fabrication, Compos. Struct. 223 (2019) 110955.
[5] Y. Hu, P. Minzioni, J. Hui, S.H. Yun, A.K. Yetisen, Fiber optic devices for diagnostics and therapy in photomedicine, Adv. Opt. Mater. 12 (22) (2024) 2400478.
[6] Y. Xiong, F. Xu, Multifunctional integration on optical fiber tips: challenges and opportunities, Adv. Photonics. 2 (6) (2020), 064001-064001.
[7] K. Zhou, M.-Z. Ai, Z.-H. Qian, X.-X. Gao, Z.-H. Hu, Q. Li, L. Yuan, Z. Wang, Y.-F. Huang, T. Tu, High-sensitivity strain sensor with an in-fiber air-bubble Fabry-Perot interferometer, Appl. Phys. Lett. 113 (18) (2018).
[8] S. Liu, Y. Wang, C. Liao, G. Wang, Z. Li, Q. Wang, J. Zhou, K. Yang, X. Zhong, J. Zhao, High-sensitivity strain sensor based on in-fiber improved Fabry–Perot interferometer, Opt Lett. 39 (7) (2014) 2121–2124.
[9] C.E. Campanella, A. Cuccovillo, C. Campanella, A. Yurt, V.M.N. Passaro, Fibre Bragg grating based strain sensors: review of technology and applications, Sensors 18 (9) (2018) 3115.
[10] W. Zhao, X. Xiao, Q. Song, H. Liu, X. Huang, Y. Liu, C. Cheng, Q. Sun, Z. Yan, Real-time strain field measurement based on dense fiber Bragg gratings array, IEEE Sens. J. (2024) 37687–37695.
[11] X. Dong, H. Du, Z. Luo, J.a. Duan, Highly sensitive strain sensor based on a novel Mach-Zehnder interferometer with TCF-PCF structure, Sensors 18 (1) (2018) 278.
[12] X. Dong, Z. Luo, H. Du, X. Sun, K. Yin, Highly sensitive strain sensor based on a novel Mach–Zehnder mode interferometer with TCF-PCF-TCF structure, Opt Laser. Eng. 116 (2019) 26–31.
[13] A. Wolf, A. Dostovalov, K. Bronnikov, M. Skvortsov, S. Wabnitz, S. Babin, Advances in femtosecond laser direct writing of fiber Bragg gratings in multicore fibers: technology, sensor and laser applications, Opto-Electron, Adv 5 (4) (2022) 210055.
[14] C. Zhu, H. Zheng, L. Ma, Z. Yao, B. Liu, J. Huang, Y. Rao, Advances in fiber-optic extrinsic Fabry–Perot interferometric physical and mechanical sensors: a review, IEEE Sens. J. 23 (7) (2023) 6406–6426.
[15] K. Tian, M. Zhang, J. Yu, Y. Jiang, H. Zhao, X. Wang, D. Liu, G. Jin, E. Lewis, G. Farrell, High sensitivity, low temperature-crosstalk strain sensor based on a microsphere embedded Fabry–Perot interferometer, Sensor Actuator Phys. 310 (2020) 112048.
[16] B. Su, B. Qi, F. Zhang, L. Zhong, O. Xu, Y. Qin, Hybrid fiber interferometer sensor for simultaneous measurement of strain and temperature with refractive index insensitivity, Opt. Commun. 522 (2022) 128637.
[17] A.D. Gomes, H. Bartelt, O. Frazão, Optical Vernier effect: recent advances and developments, Laser Photon. Rev. 15 (7) (2021) 2000588.
[18] P. Yang, B. Peng, J. Ye, Novel microspherical fiber Fabry–Pérot interferometer based on the Vernier effect for micro-displacement sensing, Opt. Fiber Technol. 80 (2023) 103461.

[19] X. Liu, P. Nan, J. Zhu, Z. Li, J. Dan, W. Dang, K.-S. Lim, W. Udos, H. Ahmad, X. Liu, Ultrasensitive parallel double-FPIs sensor based on Vernier effect and Type II fiber Bragg grating for simultaneous measurement of high temperature and strain, Opt. Commun. 508 (2022) 127717.
[20] X. Yang, S. Wu, H. Cheng, J. Ma, S. Wang, S. Liu, P. Lu, Simplified highly-sensitive gas pressure sensor based on harmonic Vernier effect, Opt Laser. Technol. 140 (2021) 107007.
[21] J. Li, M. Zhang, M. Wan, C. Lin, S. Huang, C. Liu, Q. He, X. Qiu, X. Fang, Ultrasensitive refractive index sensor based on enhanced Vernier effect through cascaded fiber core-offset pairs, Opt. Express 28 (3) (2020) 4145–4155.
[22] L. Zhao, S. Hao, Y. Chen, E. Zhao, C. Xing, J. Fan, J. Tang, Simultaneous measurement of strain and temperature based on fiber sensor with Vernier effect, Opt Laser. Technol. 157 (2023) 108670.
[23] L.G. Abbas, Vernier effect-based strain sensor with cascaded Fabry–Pérot interferometers, IEEE Sens. J. 20 (16) (2020) 9196–9201.
[24] S. Zhao, Z. Cao, H. Li, W. Luo, J. Chen, Y. Fu, B. Liu, J. Lin, B. Yu, A highly sensitive temperature and strain sensor based on fiber lyot filter with vernier effect, Opt. Fiber Technol. 73 (2022) 103062.
[25] T. Nan, B. Liu, Y. Wu, J. Wang, Y. Mao, L. Zhao, T. Sun, J. Wang, Ultrasensitive strain sensor based on Vernier-effect improved parallel structured fiber-optic Fabry-Perot interferometer, Opt. Express 27 (12) (2019) 17239–17250.
[26] X.-P. Pan, H.-E. Yang, S.-R. Liu, B. Wang, M.-M. Gao, Q. Guo, Q.-D. Chen, H.-B. Sun, Y.-S. Yu, High sensitivity fiber optic strain sensor based on CFBG-FPI and vernier effect, J. Lightwave Technol. (2023) 6831–6837.

S1：SI production repeatability

Four sensor samples are fabricated and the measured sums of axial bubble length, bubble wall thickness, and longitudinal bubble length are obtained, as shown in Table S1. The fabrication of this strain sensor is reproducible yet still has certain limitations. Similar sensitivity can be achieved by preparing RI with different FSR_R, resulting in different amplification factor M.

Table S1: SI production repeatability and related parameters.

Name	Micrographs	Axial bubble length	Upper bubble wall thickness	Bottom bubble wall thickness
SI_1	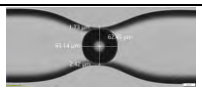	63.14 μm	1.73 μm	2.42 μm
SI_2	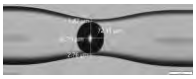	62.79 μm	5.87 μm	2.76 μm
SI_3	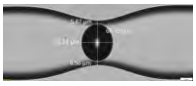	56.24 μm	5.87 μm	6.56 μm
SI_4	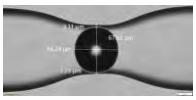	66.27 μm	3.11 μm	1.73 μm
Mean	—	62.11 μm	4.145 μm	3.3675 μm
Standard deviation	—	4.214490875 μm	2.07 μm	2.171042376 μm

S2：Correlation study of sensor parameter variations with strain sensitivity and temperature sensitivity.

The strain response of the sensor based on the vernier structure is primarily determined by the interferometer structure, and therefore, this analysis focused on the SI. The strain sensitivity of the sensors is obtained by experiments on SI_1-SI_4 in a room temperature under applied strain ranging from 0 to 600 με with the incremental steps of 100 με, as shown in Fig. S1. The experimental results show that the sensitivity of the sensor is exclusively related to the bubble wall thickness, while exhibiting no correlation with the cavity length. The thinner the bubble wall thickness, the higher the sensitivity.

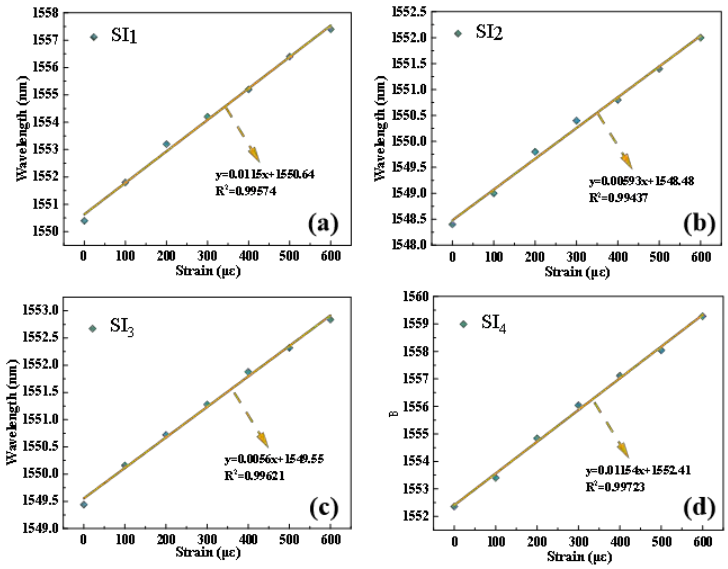

Fig. S1 Strain sensitivity of the : (a) SI_1, (2) SI_2, (3) SI_3, and (4) SI_4.

In order to form a vernier structure, reference interferometers with different FSR are matched for SI_1-SI_4, respectively. The fabricated devices are subjected to strain-testing experiments in a room-temperature environment, while the temperature characteristics of the sensors are systematically evaluated to validate sensor performance. The temperature sensitivity of the sensors is obtained by applying 25-200 °C in steps of 25 °C as shown in Table S2. The experimental results demonstrate that the temperature sensitivity of the dual FPIs sensors prepared exclusively using SMF and fiber fusion splicing techniques remains independent of the structure. The complete experimental data and analysis have been included in the Supplementary Material.

Table S2: Strain sensitivity and temperature sensitivity based on vernier structure sensors.

Name	Micrographs of RI	Strain sensitivity after paralleling	Temperature sensitivity after paralleling
RI_1	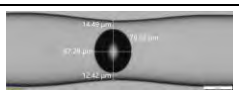	133.43 pm/με	3.85 pm/°C
RI_2	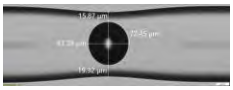	108.66 pm/με	3.26 pm/°C

RI_3	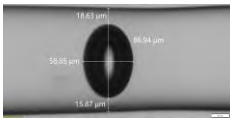	130.52 pm/με	4.59 pm/°C
RI_4	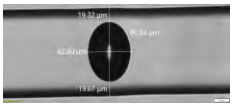	129.7 pm/με	3.26 pm/°C